Title

The effects of age and dysfunction on meibomian gland population dynamics.

Permalink

https://escholarship.org/uc/item/1z18n6sm

Authors

Wiedemann, Julie

Kashgari, Ghaidaa

Lane, Shelley

et al.

Publication Date

DOI

Peer reviewed

The effects of age and dysfunction on meibomian gland population dynamics

Julie Wiedemann[a], **Ghaidaa Kashgari**[b], **Shelley Lane**[c], **Brian C. Leonard**[d,e], **Kelly E. Knickelbein**[d], **Bogi Andersen**[a,b,*], **James V. Jester**[c,**]

[a]Mathematical, Computational and Systems Biology (MCSB) Program, University of California, Irvine, Irvine, CA, USA

[b]Department of Biological Chemistry and Medicine, School of Medicine, University of California, Irvine, Irvine, CA, USA

[c]Department of Ophthalmology and Biomedical Engineering, University of California, Irvine, Irvine, CA, USA

[d]Department of Surgical and Radiological Sciences, School of Veterinary Medicine, University of California, Davis, Davis, CA, USA

[e]Department of Ophthalmology & Vision Science, School of Medicine, University of California, Davis, Davis, CA, USA

Abstract

Purpose: While meibomian gland dysfunction (MGD) is widely recognized as a major cause of evaporative dry eye disease, little is known about normal gland differentiation and lipid synthesis or the mechanism underlying gland atrophy and abnormal lipid secretion. The purpose of this study was to use single-cell and spatial transcriptomics to probe changes in cell composition, differentiation, and gene expression associated with two murine models of MGD: age-related gland atrophy in wild-type mice and altered meibum quality in acyl-CoA wax alcohol acyltransferase 2 (*Awat2*) knockout (KO) mice.

Methods: Young (6 month) and old (22 month) wild type, C57Bl/6 mice and young (3 month) and old (13 month) Awat2 KO mice were used in these studies. For single-cell analysis, the tarsal plate was dissected from the upper and lower eyelids, and single cells isolated and submitted to the UCI Genomic Core, while for the spatial analysis frozen tissue sections were shipped to Resolve

Biosciences on dry ice and sections probed in duplicate using a meibomian gland specific, 100 gene Molecular Chartography panel.

Results: Analysis of gene expression patterns identified the stratified expression of lipogenic genes during meibocyte differentiation, which may control the progressive synthesis of meibum lipids; an age-related decrease in meibocytes; and increased immune cell infiltration. Additionally, we detected unique immune cell populations in the *Awat2* KO mouse suggesting activation of psoriasis-like, inflammatory pathways perhaps caused by ductal dilation and hyperplasia.

Conclusion: Together these findings support novel mechanism controlling gland function and dysfunction.

Keywords

Meibomian gland; Age-related meibomian gland dysfunction; Single cell RNA sequencing; Spatial transcriptomics; Awat2 knockout mouse

1. Introduction

The eyelid is a specialized skin appendage that protects the eye from trauma, excessive light, and desiccation through blinking and closure. Covered by the epidermis on the outside and the conjunctival epithelium on the inside, each eyelid contains 20–30 lipid-secreting, holocrine meibomian glands embedded in the tarsal plate, a dense connective tissue matrix between the eyelid muscle and the conjunctiva. Each gland contains a central duct that spans the length of the gland and opens at the anterior eyelid margin onto the mucocutaneous junction, where the dry, keratinized epidermis meets the moist non-keratinized conjunctiva [1]. Interspersed along the central duct, short ductules connect to 200–300 μm diameter globular acini that synthesize and release lipid into the duct. The synthesis of lipid or meibum is coordinated with the differentiation and migration of meibocytes from the basal acinar compartment toward the center of the acinus, where they fill with membrane-bound lipid droplets, activate a cell death program, lyse, and liberate meibum into the duct. During blinking, the eyelid muscles compress the meibomian glands and passively push meibum out onto the eyelid margin [2], where it spreads over the tear film and functions to retard aqueous tear evaporation and prolong tear film breakup time [3].

Meibomian gland dysfunction (MGD) with gland dropout and altered meibum quality is common in patients with dry eye disease, an ocular surface disorder with a prevalence of 39–50 % in the U.S. population [4-7]. Given that a third to half of the patients visiting optometrists and ophthalmologists show signs of MGD and complain of dry eye symptoms [5], there is a growing interest in understanding the cellular and molecular mechanisms of MGD and its role in dry eye disease. It is generally thought that MGD involves hyperkeratinization or squamous metaplasia of the ductal epithelium, followed by duct obstruction, dilation, and a 'disuse atrophy' of the gland [1,8]. Clinical studies show that dry eye disease is highly correlated with age and coincides with loss or atrophy of meibomian glands and changes in meibum quality [9]. Importantly, aging human meibomian glands show a 50 % loss in the proliferative capacity of acinar meibocytes (in >60 years old), coupled with decreased PPARγ receptor signaling, which is required for meibum synthesis

[10]. Atrophy or loss of the meibomian glands have also been identified in old mice, making the aging mouse a potential model for understanding the effects of age on meibomian gland structure and function [11]. More recently, transgenic mice with targeted deletions of genes expressing key enzymes involved in meibum lipid synthesis have been shown to phenotypically present with MGD. These include the acyl-CoA wax alcohol acyltransferase 2 (*Awat2*) knockout (KO) mouse that lacks the synthesis of wax esters, one of the two major components of meibum lipids [12], leading to increased meibum viscosity, ductal dilation, and an evaporative dry eye phenotype.

Overall, we know little about the mechanisms controlling meibomian gland renewal and differentiation and how these mechanisms change with MGD. The only single-cell transcriptomic publication on the normal meibomian gland focused predominantly on cells expressing genes associated with lipid synthesis [13]. In the present study we performed single-cell and spatial transcriptomic experiments to discover fundamental changes in meibomian gland differentiation and renewal as affected by MGD caused by age and abnormal meibum lipid synthesis. Through trajectory analysis we discovered growth and transcription factors potentially directing meibocyte and ductal differentiation, and we identified immune cell infiltration and immune mechanisms that may influence meibomian gland function.

2.   Materials and methods

2.1.   Experimental design

For this study, we used C57Bl/6 mice and an *Awat2* KO mouse on the C57/Bl6 background. The *Awat2* KO mice were obtained from the Mutant Mouse Resource & Research Centers (https://www.mmrrc.org/catalog/sds.php?mmrrc_id=43484) at The University of California, Davis. Heterozygous females ($Awat2^{+/-}$), homozygous females ($Awat2^{-/-}$), and hemizygous males ($Awat2^{-/y}$) were expanded and characterized in our lab, and shown to have markedly dilated meibomian gland orifices and ducts with thick white paste-like meibum emerging from the meibomian gland orifices. All animal procedures were approved by the University of California Irvine, Institutional Animal Care and Use Committee (AUP 23–066).

For scRNA-seq, we performed two separate runs. In the first run, we used six WT, 6-month-old, male C57Bl/6 mice, which we divided into two groups of three. In the second run, we used eight mice, including four 6-month-old, male *Awat2* KO mice and four WT, C57Bl/6 litter mates. The animals were initially sedated with Ketamine prior to cervical neck dislocation, and then the upper and lower eyelids of both eyes were processed for cell isolation and submission to the UCI Genomics Core.

For the spatial transcriptomics, we performed a preliminary run to test the ability of the Resolve Biosciences Molecular Cartography technology to identify a set of 100 transcripts targeted for skin to detect transcripts in eyelid tissue containing lipids. For this test, the left and right upper eyelids from a 6-month-old, male C57Bl/6 mouse were embedded in Tissue-Tek O.C.T. Compound (Sakura Finetek, USA, Torrance, CA) oriented for coronal sections starting at the eyelid margin. Blocks were then shipped on dry ice to Resolve Biosciences. In the second run, we used four female *Awat2* KO mice, 3 and 13 months of

age, and four female WT C57Bl/6, 6 and 22 months of age. Animals were sacrificed and the eyelids embedded in O.C.T Compound oriented for sagittal sections through the orifice and central duct of the meibomian gland. Blocks were carefully trimmed so the block face fit the dimensions of the Molecular Cartography slide, and one section from each mouse eyelid (eight sections total) were placed on the same slide. Two separate slides were then shipped on dry ice to Resolve Biosciences.

2.2.   Tissue collection and single-cell isolation

We collected eyelids and placed them in ice cold, sterile, phosphate buffered saline with a pH of 7.2. Individual eyelids were then dissected to remove the tarsal plate using a number 11 Bard-Parker scalpel to separate the tarsus from the underlying muscle and epidermis. After isolation, the tissue was minced and then placed in 500 μl of PBS containing 0.2 % collagenase (Gibco, cat# 17028-029) and 0.05 % hyaluronidase (Worthington, Cat# LS02592) in DMEM (Gibco, Cat# 31600-026). Tissues were nutated for 2 h at 37°C, spun down at 700cf for 5 min and then resuspended in 500 μl of 0.25 % Trypsin-EDTA (Gibco, Cat# 25200-056), nutated for another 5 min at 37°C, and then blocked using 500 μl of 0.25 % soybean trypsin inhibitor (Gibco, Cat# 17075-029) in PBS. Single cells were then spun down at 700cf and resuspended in 500 μl of DMEM. Finally, cells were filtered through a 250 μm filter, washed with DMEM, transferred to Eppendorf tubes on ice, and submitted to the UCI Genomics Core.

2.3.   Single-cell RNA sequencing and analysis

The UCI Genomics Core team constructed libraries using a $10 \times$ Genomics Chromium instrument and then used a Illumina NovaSeq 6000 sequencer to generate 150 bp paired-end reads. Raw sequencing data were demultiplexed and processed using Cellranger ($10 \times$ Genomics version 3.1.0) using a mm10-2020-A reference provided by $10 \times$ Genomics. Preliminary analysis and visualization of the single-cell datasets were performed using Seurat [14] in R. For all datasets, we detected and removed cells with <200 and >6000 genes and >5 % mitochondrial genes. We performed an integrated analysis of the four datasets, normalizing separately for each dataset, and then we selected 2000 informative features and performed integration using the FindIntegrationAnchors function. Cells were visualized using the UMAP algorithm. Gene ontology enrichment analysis of the genes was performed using enrichR [15] and visualized in R.

Gene and probability scores.—We calculated the scores for a group of genes associated with different cell-cycle phases using CellCycleScoring in Seurat. The gene lists for the G2M and S phase were the Seurat default.

Trajectory analysis.—Monocle trajectories were calculated using Monocle2 [16].

Further analysis.—Cell-cell similarity between meibomian gland clusters and keratinocyte clusters for the three sites was computed on the integrated matrix using MetaNeighbor [17]. Transcription factor analysis for the meibomian gland was conducted using SCENIC [18].

2.4.   Spatial transcriptomic analysis

In the two spatial transcriptomic experiments, we used sets of 100 probes, which are listed in Table S1.We created the Molecular Cartography images with probes in ImageJ using the Polylux plugin from Resolve BioSciences. We carried out cell segmentation with a combination of Cellpose [19], to segment nuclei based on the DAPI signal, and Baysor [20], to identify cell segmentation boundaries using the default pipeline from the Resolve portal. Further analysis was performed using Seurat [14]. For all datasets, cells with an area of $<10\mu m^2$, cells without transcripts, and cells containing <2 genes were removed. For each experiment, datasets were merged, clustered, and visualized in Seurat. Giotto [21] was used to identify modules of spatially coexpressed genes and cell neighborhoods.

2.4.1.   GEO submission—All single cell and spatial transcriptomic data has been submitted to NIH Gene Expression Omnibus at GSE261036.

3.   Results

3.1.   Single-cell transcriptomics of the murine eyelid

To investigate abnormalities in MGD, we first used single-cell RNA sequencing (scRNA-seq) to define cell types and states of the healthy adult mouse tarsal plate. We removed the meibomian gland-containing tarsal plate (Fig. 1A and B) and isolated single cells. After quality control and integration in Seurat [22], the dataset consisted of 16,922 cells and 23,173 genes from three different replicate samples (Fig. S1A). Through an unsupervised clustering analysis, we identified 22 cell clusters that could be organized into eight different cell groups: 1) meibomian gland, including ductal epithelia and meibocytes; 2) conjunctival epithelia; 3) hair follicle epithelia, including inner root sheath and cortex/cuticle; 4) fibroblasts, including dermal papillae and dermal sheath; 5) immune cells, including T cells, macrophages, lymphoid cells, and dendritic cells; melanocytes; 7) pericytes; and 8) endothelial cells (Fig. 1C). The proportion of these cell groups were consistent across the three samples (Fig. S1B). We determined the annotations for each cluster by the expression of established marker genes for each cell type, as well as the top marker genes for each cluster (Fig. 1D and Fig. S1C). *Col1a1* expression identified fibroblasts, with coexpression of *Col1a1* and *Acta2* marking the dermal sheath, and coexpression of *Col1a1* and *Corin* marking the dermal papillae. Expression of *Mki67* identified three populations of cycling cells, including hair follicle, conjunctiva proliferating progenitors (CJ-PP), and meibomian gland meibocyte and duct proliferating progenitors (Meib/Duct-PP). *Lhx2* was used as a general marker of the hair follicle, with *Krt73* marking the inner root sheath and *Krt35* marking the cortex/cuticle. The conjunctiva was marked by general expression of *Cldn4*, with specific expression of *Krt13* in the differentiated conjunctiva. In the meibomian gland, *Ly6d* was highly expressed in the ductal epithelial clusters, and *Plin2* was highly expressed in the meibocytes. One cluster of immune cells, T cells/lymphoid cells, specifically expressed T cell marker *Cd3e*, while the other cluster, macrophages/dendritic cells, expressed *C1qa*, a monocyte marker. Pericytes were marked by expression of *Rgs5,* endothelial cells by *Cdh5,* and melanocytes by *Mlana*.

Cell-cycle scoring confirmed the presence of three highly proliferative cell-type subsets: hair follicle cells (HF-III), the basal conjunctiva (CJ-PP), and undifferentiated meibocyte/ductal cells (Meib/Duct-PP) (Fig. 1E). Their presence was consistent with the pattern of expression of proliferation marker *Mki67* (Fig. 1D). Whereas other clusters generally consisted of different proportions of all three cell-cycle states, cells in these three clusters were exclusively in G2M or S phase.

3.2.   Distinct proliferating progenitors for duct and acini

Subclustering of the 3741 meibomian gland cells resulted in the formation of seven clusters: four constituting ductal epithelia and three constituting lipid synthesizing meibocytes that reside in the gland acini. The subclusters were consistent across the three replicates (Fig. 2A; Fig. S2A). The ductal epithelia populations were marked by expression of *Cenpf, Ube2c, and Top2a* in proliferating progenitors; *Tmem45a, Mfge8, and Ly6d* in non-proliferating progenitors; *Klk8, Krt1,* and *Krt10* in the keratinized differentiated ductal epithelium; and *Krt79, Ly6g6c, and Krtdap* in the non-keratinized differentiated ductal epithelium. The meibocyte populations were marked by the expression of *Pclaf, Hist1h2ap,* and *Hist1h1b* in proliferating progenitors; *Plin2, Ccn1,* and *Klf6* in non-proliferating progenitors; and *Scd1, Dhcr24,* and *Fdps* in differentiated meibocytes (Fig. 2B). The Meib/Duct-PP population identified in the clustering of the whole dataset (Fig. 1C) separated into two distinct clusters, one associated with the ductal epithelia and the other with meibocytes (Fig. 2A). Although both proliferating progenitor cell populations express high levels of proliferation-associated genes, including *Mki67* and *Cenpf,* the cycling meibocyte and ductal progenitors exhibited key differences, with the ductal progenitors marked by upregulation of genes such as *Krt15*, *Ly6d*, and *Alox12e*, and the meibocyte progenitors marked by upregulation of meibocyte-associated genes including *Plin2, Psph*, and *Hmgcr* (Fig. S2B). Furthermore, these two cycling populations remained separated after cell-cycle regression, indicating they were likely two biologically distinct populations (Fig. S2C).

In an analysis of the meibomian gland populations using MetaNeighbor [17], we validated the consistency of the identified clusters across the three samples and demonstrated the marked differences between the ductal epithelia and meibocyte clusters overall (Fig. 2C). Additionally, this analysis further supports the existence of two separate cycling populations, as the cycling meibocyte progenitors are far more similar to both the non-cycling meibocyte progenitors and differentiated meibocytes than they are to the ductal epithelia populations. Conversely, the cycling ductal progenitor population is more similar to the other three ductal epithelia clusters than to the meibocyte clusters.

3.3.   Distinct differentiation branches for duct and acini

Patterns of keratin expression in the duct cells and meibocytes further validated the notion of two distinct meibomian gland differentiation branches. We found that the keratinized differentiated duct and the ductal progenitors highly express basal marker *Krt5*, which is relatively lowly expressed in the non-keratinized differentiated duct (Fig. 2D). Additionally, the non-keratinized portion of the duct specifically expresses *Krt6a*, whereas the keratinized portion of the duct expresses *Krt1* (Fig. 2D). We also identified differences in the expression of *Krt5* and *Krt14*; whereas *Krt14* was highly expressed throughout the meibomian gland

populations, *Krt5* expression dropped off with non-keratinized ductal differentiation (Fig. 2D). *Krt79* was highly expressed in both the non-keratinized differentiated duct and the differentiated meibocytes, whereas *Pparg* expression was restricted to the meibocytes and increased with differentiation (Fig. 2D). This finding that differentiated meibocytes expressed both *Krt14* and *Krt79,* but not *Krt5,* is consistent with the results of recent studies on sebaceous gland differentiation [23].

We also identified differences in the expression of lipid synthesis-associated genes, particularly the elongation of very-long-chain fatty acids gene family (Elovls). Whereas *Elovls 1*, *3,* and *6* marked mature meibocyte populations, *Elovls 4* and *7* specifically marked non-keratinized differentiated ductal epithelia (Fig. 2E). Lipid-synthesis markers *Scd1* and *Hmgcr* showed exclusive expression in the meibocytes, with progressively increasing expression from progenitor differentiated meibocytes, whereas markers of lipid synthesis *Far2, Awat2* and *Soat1* specifically marked differentiated meibocytes (Fig. 2E). However, the lack of expression of *Awat1*, as well as the relatively low expression of *Awat2* and *Scd3* in the differentiated meibocytes, indicates that the single-cell dataset was likely missing the majority of the most differentiated populations of meibocytes (Fig. 2E). This limitation may also explain the absence of other lipid enzymes including Elovl4 and Elovl7 that have been noted to be highly expressed in meibocytes [24]. Since maturation of meibocytes and the synthesis of lipids likely causes a dramatic change in the cell density or cell fragility, capturing this population may require a specialized approach not consistent with standardized single cell transcriptomic analyses.

Ordering the cells of the meibomian gland into a pseudotime trajectory using Monocle [25] revealed a split-differentiation trajectory, with one side of the trajectory comprised of meibocytes, with the most differentiated meibocytes at one end, and the other side comprised of ductal epithelia, culminating in the non-keratinized differentiated duct (Fig. 2F). The two branches of the meibomian gland trajectory each had actively cycling cells at its base, further supporting the presence of two transcriptionally distinct proliferating populations, one in the acinus and the other in the duct. The small number of cells that connected the two branches were highly similar to the non-proliferating meibocyte progenitors. Projection of meibocyte markers *Plin2* and *Soat1*, as well as duct markers *Ly6d* and *Sbsn*, further supported this dual differentiation trajectory, while the expression of *Mki67* demonstrated that the two branches of the trajectory were driven by proliferation (Fig. 2G). The keratinized differentiated duct population, as marked by *Klk8*, appeared to be concurrent in pseudotime with the ductal progenitors, indicating a potentially parallel path of differentiation within the duct (Fig. 2G). The expression of distinct transcription factors and gene ontologies peak at the early, mid, and late meibocyte (Fig. 2H and I) and duct (Figs. S2F-I) lineages.

3.4. Distinct transcriptional networks in the duct and acini differentiation branches

Using SCENIC [18], we found enrichment of distinct transcription factor networks in the meibocyte and ductal populations (Fig. 3A and B), further supporting the concept of distinct cellular lineages (Fig. 2C). In the meibocyte branch of the pseudotime trajectory, we identified early activation of networks associated with lipid synthesis, namely *Pparg*

and *Cebpa*, whereas the *Stat1* network was activated later in pseudotime (Fig. 3B). By contrast, the ductal epithelia populations were marked by activation of networks associated with epithelial differentiation, including *Fos, Mafb*, and *Klf4* (Fig. 3A and B), and the Elf5 network was activated in the non-keratinized differentiated duct late in pseudotime. Additionally, the keratinized differentiated duct portion of the pseudotime trajectory was specifically marked by the activation of the *Sox21* network (Fig. 3B). CellChat [26] analyses for cell-cell communications predicts multiple active signaling pathways (Fig. 3C), in which meibocyte and ductal progenitors have the highest outgoing signal strength and the ductal epithelia II has the highest incoming signal strength (Fig. 3D).

3.5. Spatial transcriptomics mapping of cell states and types in the murine eyelid

To further characterize the meibomian gland and localize the populations identified in the single-cell data, we used Molecular Cartography (Resolve Biosciences), which allows for spatial RNA analysis of a panel of 100 genes (Table S1). We generated gene cell matrices for the two samples based on the number of transcripts within cell segmentation boundaries, using a combination of Cellpose [19] and Baysor [20]. After quality control (Fig. S3A), the dataset consisted of 14,576 cells. Through unsupervised clustering, we defined 13 cell states (Fig. 4A), which are highly consistent between the two replicates (Figs. S3B and C). These included four fibroblast populations: fibroblast 1, which was *Col1a1*-high; fibroblasts 2 and 3, which was *Vim*-high; and fibroblast 4, which was marked by expression of *Txnip* and *Igfbp5* (Fig. 4B).

We identified three meibomian gland clusters: MG1, the most undifferentiated, expressing *Apoe* and *Krt14*; MG2, intermediary cells, expressing *Mgst1* and *Tmcc3*; and the most differentiated MG3, expressing *Cd36* and *Btg2*. We detected a general immune cluster, marked by *C1qa,* and two hair follicle clusters, marked by *Lef1* (HF1) and *Cxcl14* (HF2), respectively. We also identified three conjunctiva clusters (CJ1-3), all marked by *Krt15*, including one cluster, CJ2, that incorporated both conjunctiva and epidermis (Fig. 4B).

In addition to unbiased clustering in Seurat, we used Giotto [21] to identify spatially coexpressed modules of genes. With the k-NN algorithm, we identified nine clusters of coexpressed genes, which captured undifferentiated (cluster 3) and differentiated (cluster 2) meibocytes; two clusters of fibroblasts, one closer to the meibomian gland (cluster 1) and the other in the center of the eyelid (cluster 7); immune cells (cluster 6); and the conjunctiva (cluster 9; Figs. S3D and E). Additionally, through spatial coexpression (Figs. S3D and E), we identified both the inner hair follicle (cluster 5) and outer hair follicle (cluster 8), as well as the dermal papillae (cluster 4), which did not form a distinct cluster without incorporating spatial information (Fig. 4A).

Reclustering of the conjunctiva revealed four clusters: one general basal cluster, a second basal cluster specifically marked by *Serpina2n* and *Cxcl16*, and two differentiated populations (Fig. S3F). Whereas CJ diff 1 was located closer to the basal populations and served as an intermediate step in differentiation, CJ diff 2, the most superficial cluster, specifically expressed a number of genes, including *Plac8* (Fig. 4C; Figs. S3F and G). The conjunctiva populations all expressed *Krt15* (Fig. 4B), consistent with the scRNA-seq of conjunctiva cell populations (Fig. S1C). However, specific markers of CJ diff 2, the most

differentiated spatial cluster, did not show a clear pattern of expression in the scRNA-seq (Figs. S3H and I), indicating that the scRNA-seq data was likely missing the differentiated conjunctival epithelia that were successfully captured in the spatial data. Although a comparitively few number of immune cells were identified ($n = 338$), through the projection of individual transcripts for select immune markers, we identified four types of immune cells: *C1qa,* expressing macrophages; *C209a,* expressing dendritic cells, which comprised the majority of the immune cells identified; and smaller numbers of *Cd7+* T cells (Fig. 4D). Our spatial-transcriptomic approach was thus sensitive enough to identify both rare populations of immune cells and populations of differentitated cells that were not captured in the single-cell data. Furthermore, the spatial approach highlighted the heterogeneity of eyelid fibroblasts and their preferential location in the eyelid.

3.6. Gradual differentiation in the meibomian gland

By subclustering meibomian gland cells in the Molecular Cartography experiment, we identfied five meibomian gland populations, separating out the basal duct population, as well as an *Mki67+* cycling basal population, which was consistent across the two replicates (Fig. 5A; Figs. S3J-L). *Apoe* marked both the basal meibocyte and ductal population, but *Igfbp2* was specifically expressed in the meibocytes, and *Krt15* was specifically expressed in the duct, consistent with the scRNA-seq data (Fig. S3L). Whereas proliferative cells appeared to be scattered throughout the gland, a clear pattern of stepwise or stratified differentiation in individual acini was observed with cells sequentially expressing *Igfbp2, Far1, Far2,* and *Awat2* as cells moved from the basal to suprabasal compartments (Fig. 5B and C). Specifically, *Awat2* transcripts were identified only in the most differentiated acinar cells (Fig. 5C), consistent with the location of *AWAT2* protein localization (Fig. 5B).

Within the spatial data, we used Spearman correlation of coexpressed genes in both replicates (Fig. 5E) to demonstrate the consistency of the two replicates and confirm the overall similarity in the transcriptional profile within general cell types for the fibroblasts, meibomian gland, conjunctiva, and hair follicle. To more comprehensively examine the spatial distribution of the identified cell populations, we built a Delauney network (Fig. S3M) and constructed cell neighborhoods of spatially localized cell types based on observed interactions (Fig. 5F; Fig. S3N). We found that the conjunctiva clusters were most closely associated with each other (Fig. 5F; Fig. S3O). Within the fibroblast populations, fibroblast 1 and fibroblast 4 were the most spatially distinct from each other, with fibroblast 1 being more closely associated with hair follicle populations. The remaining populations, fibroblasts 2 and 3, were both found near the meibomian gland. Immune cells were also localized near fibroblasts and basal meibocytes (Fig. 5F; Fig. S3O). In the meibomian gland, consistent with the stages of differentiation, MG basal cells were localized close to MG diff 1, which was in turn close to MG diff 2. The MG basal proliferating cluster was also close to both MG basal and MG diff 1 (Fig. 5F; Fig. S3O). Notably, the MG duct was found to be most closely associated with the most differentiated meibocyte cluster, MG diff 2, which is consistent with its role in forming the short ducts connected to the terminal differentiating region on the acini where meibocytes disintegrate. As in the conjunctival data, the most differentiated cells of the meibocyte cluster, MG diff 2, are not present in the single-cell data (Figs. S3P-R).

3.7. A heightened immune environment in the Awat2 KO eyelid

Previous studies have shown that KO of *Awat2* blocks the ability of the meibomian gland to synthesize wax esters [12], which normally comprises 40 % of the meibum lipid, resulting in an increased proportion of cholesterol esters, the other major lipid component. Given that cholesterol esters have a higher melting point than wax esters, this change in meibum composition leads to meibum thickening and increased viscosity with retention of meibum in the meibomian gland duct. As seen by histology, meibum retention results in dramatic dilation of the duct, suggesting ductal obstruction, a common feature of MGD in patients with evaporative dry eye disease (Fig. 6A and B).

To identify transcriptomic alterations caused by ductal obstruction of the meibomian glands, we integrated our single-cell data from *Awat2* KO mice with the comparable wild-type (WT) tarsal plate dataset, resulting in 29,277 cells (Fig. 6C; Fig. S4A). The cell types we identified in this integrated dataset was largely consistent with those in the WT (Fig. 6C; Fig. S4B). However, there was an emergence of a KO-exclusive, neutrophil population (Fig. 6D), which expresses canonical neutrophil markers, including *S100a8, S100a9,* and *Mmmp9* (Fig. S4C). Additionally, we found a marked increase in the proportion of T cells in the *Awat2* KO tarsal plate, supporting the concept of a heightened immune environment in the KO eyelid. We also detected a marked increase in meibomian gland ductal epithelial cells (Fig. 6D; Fig. S4F). In comparison, the number of meibocytes remained largely unchanged, indicating that the expanded meibomian gland was due to hyperproliferation of the duct. This ductal expansion was largely restricted to the ductal progenitors (Figs. S4F and G), and the keratinized duct population was in fact reduced in the *Awat2* KO eyelids.

In addition to changes in cell type composition in the eyelids of the *Awat2* KO mice, we also identified alterations in inflammatory signaling. Within epithelia cells, we detected expression of *Il23a*, specifically upregulated in the non-keratinized ductal epithelial cells, whereas *Lcn2* was upregulated in all meibomian gland cell clusters (Fig. 6E) and in all conjunctival cell clusters (Fig. S4H). Interestingly, both factors have been implicated in inflammatory skin disease, with upregulation of *Il23a* characteristic of psoriatic lesions. *Lcn2* is similarly upregulated in psoriatic skin lesions, where it is associated with neutrophil recruitment [27], consistent with our finding of an *Awat2* KO specific neutrophil population (Fig. 6D). Within the immune cells, we detected upregulation of *Il17a* in the eyelid T cells of the *Awat2* KO (Fig. 6F), a finding that parallels upregulation of Il17a in psoriasis T cells, further supporting the concept that the *Il23/Il17* axis of inflammatory signaling may contribute to MGD.

General upregulation and down regulation of gene ontology terms are presented in Fig. 6H and fig. S4J and K, respectively. We also identified cell-type specific differences in gene expression, including *Krt6a*, one of the top upregulated genes, which was particularly upregulated in the conjunctiva and the ductal epithelia (Fig. 6G). Among the top upregulated genes in *Awat2* KO conjunctiva was *S100a9* (Fig. 6G), a gene that has recently been shown to induce psoriasiform skin inflammation through induction of type 3 immune response and IL-23 signaling [28]. Additionally, gene ontology enrichment for the conjunctiva highlights various neutrophil-associated terms (Fig. 6H), in line with the increased neutrophil infiltration seen in the *Awat2* KO. In the meibomian gland, we also identified upregulation

of *Fabp5* and *Lcn2* and enrichment of gene ontology terms associated with regulation of immune processes and metabolism. In fibroblast populations, upregulation of heat shock proteins *Hspa1a* and *Hspa1b* and downregulation of cell cycle-associated genes, including *Tubb2a, Tuba1a,* and *Cdkn1c,* were also identified in the *Awat2* KO, along with enrichment for terms associated with the extracellular matrix and regulation of proliferation.

3.8. Altered differentiation of the meibomian gland in Awat2 KO

To identify alterations of transcriptional pathways in the differentiating meibomian gland of the *Awat2* KO mice, we ordered the meibomian gland cells into a pseudotime trajectory using Monocle [25]. As in the WT (Fig. 2D), we observed a split differentiation trajectory, with one side of the trajectory comprised of meibocytes and the other comprised of ductal epithelia (Fig. 6I). In terms of differentially expressed genes over pseudotime, we detected the expected absence of *Awat2* expression and the specific downregulation of *Mia* in the differentiated meibocytes (Fig. 6J). In the duct, we identified the downregulation of *Ccl27a* (Fig. 6J), a cytokine widely expressed in homeostatic skin that is downregulated in inflammatory skin diseases such as psoriasis [29,30] and hidradenitis suppurativa [31]. Finally, we identified upregulation of *Hif1a* in the ductal epithelial lineage and upregulation of *Fabp5* in both the meibocyte and ductal lineages, with earlier expression detected in less differentiated cells in the *Awat2* KO mice (Fig. 6J).

3.9. Expanded meibomian glands and altered meibogenesis in Awat2 KO

To validate the scRNA-seq findings spatially, we created a targeted gene panel based on canonical cell markers, lipid-associated genes, and differentially expressed genes in the single-cell data (Table S1). The spatial dataset consisted of eight eyelids from eight different mice encompassing four conditions: young WT, old WT, young *Awat2* KO, and old *Awat2* KO, with duplicates for each condition. We generated gene cell matrices for each sample based upon the number of transcripts within cell segmentation boundaries, with more than 85 % of transcripts mapping to cells consistently across each sample (Fig. S5A). After quality control, the merged dataset consisted of 36,668 cells. We identified the following six overarching cell types: meibomian gland, including meibocytes and duct; fibroblasts; hair follicle; conjunctiva; Cd74 high/immune; and epidermis (Fig. 7A and B). These annotations were based on the expression of canonical markers (Fig. S5B). The most marked difference we identified in cell type composition was in the expanded meibomian gland population in the *Awat2* KO compared to the WT (Fig. 7B; Fig. S5C).

To further characterize the differences within the meibomian gland, we subclustered the meibomian gland population, a total of 9592 cells. This resulted in the formation of five clusters: MG basal/duct, marked by *Igfb2* and *Apoe;* MG diff 1, marked by *Far2*, *Scd3*, and *Soat1*; MG diff 2, marked by *Plin2*, *Cd36*, and high levels of *Awat1*; MG diff 3, which was similarly marked by *Plin2* and *Cd36*, but specifically expressed *Awat2*; and MG Ccr2, marked by a high expression of *Ccr2* and lower levels of MG diff 1 (Fig. 7C and D). In the three differentiated populations, there was a sequential differentiation from MG diff 1, which was located closer to the MG basal/duct cells, into either MG diff 2, which was enriched in the *Awat2* KO, or MG diff 3, which was enriched in the WT (Fig. 7E). The MG diff 3 population had high *Awat2* expression and represented the normal progression of meibocyte

differentiation, which was absent in the *Awat2* KO (Fig. 7E and F). Additionally, there was a distinct population of *Ccr2*-expressing cells that were enriched in the *Awat2* KO, which, like MG diff 1, also expressed *Soat1, Far2,* and *Scd3* (Fig. 7E and F; Figs. S5F and G). However, based on expression in the single-cell data, these cells are likely immune cells that are localized within the meibomian gland (Fig. S5E).

As was the case in the previous spatial experiment, there was a stratification of the meibocytes, which turn on and off lipid biogenesis and other associated genes in sequence as they differentiate. Across all conditions, the meibomian gland was divided into basal cells marked by *Igfbp2*, differentiated meibocytes expressing *Elovl3,* and terminally differentiated meibocytes expressing *Awat1* and *Awat2* in the WT and *Awat1* in the *Awat2* KO (Fig. 7G). This general pattern of differentiation held true with other lipid-associated genes, as we detected sequential expression of basal markers *Krt5* and *Igfbp2*, followed by expression of *Far2* and *Soat1* in early-differentiating meibocytes, and *Far1 and Awat2* expression in late-differentiating meibocytes (Fig. S5H). However, within the confines of the consistent meibocyte cell stages identified across conditions, we identified marked gene expression differences in the *Awat2* KO. Notably, we detected compensatory upregulation of *Awat1* in MG diff 2, the terminally differentiated meibocytes of the *Awat2* KO (Fig. 7G; Fig. S5H). We observed consistent upregulation of various meibomian gland-specific spatial markers in the differentiated meibocytes of the *Awat2* KO, including *Plin2*, *Elovl3*, *Far1*, and *Egr2* (Fig. S5H). Additionally, we detected slight upregulation of *Krt6a* (Fig. S5H) in the MG basal/ duct population that appeared confined to the duct spatially, and we detected upregulation of *Fabp5* expression in the *Awat2* KO, particularly in MG basal/duct, which is consistent with our findings in the single-cell data (Fig. 6G; Fig. S5H). Thus, although the general pattern of meibocyte differentiation appeared across all conditions, we could identify key alterations in the transcriptional pathways of meibogenesis in the spatial data.

3.10. Heightened immune activation in MGD and age

We next spatially characterized the general changes in the inflammatory environment of the eyelid during MGD. At the mucocutaneous junction, we detected a specific, spatially restricted population of cells that highly expressed *S100a9* in the *Awat2* KO mice (Fig. 8A). This population of *S100a9*-expressing cells was consistent with the single-cell data, where in addition to S100a9 marking the neutrophil population (Fig. S4C), *S100a8* and *S100a9* were also specifically upregulated in the conjunctiva of the *Awat2* KO (Fig. 6G). Additionally, there was an increase in the proportion of cells expressing *Il17a* and *Il23a* in the *Awat2* KO in both young and aged mice, consistent with our findings in the single-cell data (Fig. 8B-E). These spatial results further support our finding of a psoriasis-like immune alteration mediating MGD in the *Awat2 KO* model that leads to neutrophil infiltration, as confirmed by immunohistochemistry (Fig. 8F and G).

Although the number of specific immune cells was too small to be accurately captured in our general spatial clustering results, we were able to visualize the immune cell populations that were located closest to the meibomian gland in each condition, using *Cd3e* to mark T cells, *Cd209a* to mark dendritic cells, and *C1qa* to mark macrophages (Fig. 8H-K). Overall, a slightly lower proportion of cells expressed *Cd209a* in *Awat2* KO eyelids (Fig. 8I), and

there also seemed to be a reduction in T cells in the old *Awat2* KO only (Fig. 8J). Finally, we detected a higher proportion of macrophages in both old *Awat2* KO and WT mice (Fig. 8K).

In conclusion, we created a single-cell spatial atlas of meibomian glands under homeostasis and dysfunction associated with age and altered lipid synthesis. Specifically, we identified the segmental expression of genes for lipid synthesizing enzymes suggesting the stratification of meibocyte differentiation the sequential processing of lipid to form mature meibum. Additionally. we showed activation of IL23/IL17 immune pathways that are associated with altered meibum synthesis duct dilation.

4. Discussion

Much of what is known about meibomian gland growth, renewal, and dysfunction is based on the characterization of meibum lipids from normal animals, individual subjects, or patients with dry eye disease [32-36], and from subjective evaluations of meibomian gland structure and meibum lipid quality [8], combined with limited histopathological studies of eyelid tissues from severe dry eye patients [37-39]. Furthermore, our understanding of the molecular mechanisms controlling meibomian gland function has predominantly relied on cell culture studies using immortalized cells that only partially recapitulate meibomian gland biology [40-42] or on knowledge transferred from studies of sebaceous glands [1]. Here, we have explored the dynamic transcriptional landscape of the meibomian gland and its supporting cells in the eyelids of adult WT mice and compared these findings to two established models of MGD, one associated with age and the other associated with altered meibum quality, to bridge gaps in our knowledge about cellular and molecular mechanisms that regulate the meibomian gland.

Our findings suggest that there is an underlying dynamic interplay between the two major cell types present in the meibomian gland: the acinar meibocytes, responsible for the synthesis of meibum, and the ductal epithelium, responsible for the delivery of meibum to the eyelid margin. The growth and differentiation of these two cell types feature distinct transcriptional control pathways, which comprise a more complex mechanism than previously imagined, involving a dual epithelial differentiation pathway, directed toward keratinized and non-keratinized epithelium, and a spatially segregated, meibocyte differentiation pathway, leading to the sequential synthesis of unique meibum lipids. Our study also shows that alterations in these differentiation pathways can set off a type 3 inflammatory cascade that envelopes the meibomian gland and the adjacent conjunctival epithelium, potentially leading to ocular surface inflammation and dry eye disease. To explore the impact of our findings on the understanding of meibomian gland function and dysfunction, we have focused our discussion on 1) mechanism-controlling meibomian gland growth, differentiation, and dysfunction; and 2) the consequence of altered meibum quality and development of inflammation.

4.1. Mechanism-controlling meibomian gland growth, differentiation, and dysfunction

Through a single-cell transcriptome analysis, we identified two separate differentiation pathways involving the meibocytes and ductal epithelium that feature different transcription factor networks, including Pparg/Cebpa and Mafb/Klf4, respectively. Furthermore, these

two differentiation trajectories remain separate, suggesting independent stem/progenitor cell populations for acini and duct. These findings are consistent with previous lineage-tracing studies in Confetti mice, which show separate labeling of acini and ductal epithelial cells, suggesting the presence of at least two separate progenitor/stem cell populations giving rise separately to meibocytes and ductal epithelial cells [43]. These findings also support a mechanism for age-related meibomian gland atrophy involving exhaustion of meibocyte stem/progenitor cells.

For the ductal epithelium, we identified two different terminal differentiation pathways that arise from the same stem/progenitor cell population, giving rise to keratinized and non-keratinized epithelial cell populations. Differentiation along these two lineages is marked by different transcription factor networks, including Sox21 for keratinized and Elf5 for non-keratinized ducts. Partial keratinization of the meibomian gland is well known, and early animal models of hyperkeratinization have long formed the basis for an obstructive mechanism underlying MGD [44-47]. While obstructive MGD models have focused on hyperkeratinization of the gland orifice leading to direct plugging of the gland, our finding that ductal progenitor cells can differentiate along two separate pathways from the same progenitor cell population suggests that factors controlling epithelial differentiation may influence the balance between keratinized and non-keratinized epithelium deeper within the gland. An increase in keratinized ductal epithelial cells may be less responsive to cellular degradation, leading to the accumulation of non-degraded, desquamated epithelial cells and/or their debris within the duct lumen, obstructing the flow of meibum toward the lid margin rather than plugging the gland orifice. It should also be noted that that there were similar numbers of keratinized and non-keratinized differentiated ductal epithelial cells captured in our single cell data, while K10 transcripts were spatially limited to the orifice of the gland and the eyelid surface adjacent to the mucocutaneous junction. Since a limited number of keratinized ductal epithelial cells is more consistent with previous immunostaining reports [48], the equal number of keratinized/non-keratinized ductal epithelial cells derived from the same stem/progenitor cell suggests that keratinized ductal cells may populate the eyelid surface and form the skin portion of the mucocutaneous junction. Certainly, further study of these alternative mechanism is warranted, given the current interest in using keratolytics to treat MGD and dry eye disease [49].

Turning to the spatial-transcriptomics data, the expression of genes involved in lipid synthesis shows a distinct segmental pattern that stratifies differentiating meibocytes into early-phase meibocytes expressing *Soat1/Far2* and late-phase meibocytes expressing *Awat2*. This pattern of expression provides a novel insight into the synthesis of meibum, which appears to be controlled by the differentiated state of the meibocyte, as determined by its distance from the basal cell compartment. Although it has been widely recognized that meibocytes begin to accumulate lipid following migration into the acinus, it has not been known if there were differences in the types of lipids accumulated in meibocytes prior to cell disintegration and release into the meibomian gland duct. The finding that *Soat1/Far2* is expressed solely in the early differentiating meibocytes indicates that cholesterol esters and fatty alcohols, the products of Soat1 and Far2 enzymatic activity [32], may comprise the major lipids in this early differentiating cell. Later, as meibocytes move toward the duct, *Soat1* and *Far2* transcripts disappear, and expression of *Awat2* is upregulated,

leading to the synthesis of wax esters from the fatty alcohols synthesized by the earlier differentiating meibocytes. This spatial pattern in expression of *Awat2* is predicted by earlier findings showing that *Awat2* is expressed only in spheroid cultures, where meibocytes can migrate from the basal compartment into the center of the spheroid [50]. This segregation in expression was also suggested by a recent transcriptomic study in which different populations of meibocytes expressed different lipogenic genes [51].

Although it is unknown whether other sequential enzyme expression patterns exist that may impact the synthesis of meibum, the dissociated expression of *Far2* and *Awat2* seem to add additional complexity to the process of meibum synthesis and may affect meibum quality and the development of MGD. Desiccating stress is a known risk factor for MGD and dry eye, leading to a compensatory increase in progenitor cell proliferation and altered protein levels in mouse meibum [52]. Yet, if desiccating stress affects the sequential process of meibocyte differentiation, changes in the lipid composition of meibum might also be expected to lead to altered meibum quality. Certainly, further study of this newly discovered differentiation process is needed to understand its role in gland dysfunction and dry eye disease.

The spatial-transcriptomics data comparing young and old meibomian glands also showed a marked decrease in up to 50 % of meibomian gland cells. Again this is consistent with previous structural studies of mouse meibomian glands showing age-related atrophy and decreased progenitor cell proliferation rates and expression of *Pparg* [11,48,53], all supporting the idea of stem/progenitor cell exhaustion as a mechanism of age-related disease.

4.2. Consequence of altered meibum quality and development of inflammation

We used the *Awat2* KO mouse as a model for MGD resulting from altered meibum quality caused by the loss of wax esters and other lipid species. AWAT2 catalyzes the synthesis of wax esters from fatty alcohols and, with cholesterol esters, forms one of the two most prominent lipids in meibum. Loss of wax esters results in an increase in the melting point of meibum, leading to thickening and increased viscosity at body temperature, which causes plugging of the meibomian gland and a dry eye phenotype due to abnormal tear film stability and ocular surface damage [12,54]. Although the effects of *Awat2* KO on the synthesis of lipids and the development of dry eye disease have been reported, the single-cell transcriptome analysis of *Awat2* KO mice showed a distinct shift in the differentiation trajectory of meibocytes and ductal epithelial cells, which in WT mice was evenly divided but in *Awat2* KO mice was shifted in favor of ductal epithelial cells, suggesting hyperplasia of the duct. This finding was validated in the histologic data, where the ductal epithelial thickness dramatically increased from 3 to 7+ cells thick at the orifice of the gland and throughout the central duct. Although the population of meibocytes decreased only slightly, the ductal epithelial cells expanded in the relative proportion of ductal progenitor cells and differentiating non-keratinized epithelium with a marked decrease in the proportion of keratinized epithelium. These findings suggest that the response of the meibomian gland to altered meibum quality and ductal dilation was hyperplasia of the ductal epithelium in

the absence of hyperkeratinization, a finding that is contrary to what has been reported previously [12].

Other gene expression changes included decreased expression of meibocyte differentiation marker *Mia* and chemokine *Ccl27a*, as well as increased expression of *Hif1a* and *Fabp5* in the ductal epithelium. The loss of *Mia* suggests that AWAT2 may have unknown effects on meibocyte differentiation, and the decrease in *Ccl27a* and increase in *Fabp5* may be linked to effects of inflammation similar to that identified for psoriasis [29,30,55]. The enhanced inflammation previously noted in the *Awat2* KO was also captured by the dramatic increase in both the T-cell and neutrophil populations, coupled with the expression of IL-23a in the non-keratinized and progenitor ductal epithelial cells. Interestingly, upregulation of IL-23a in the skin of psoriasis patients has been linked to the recruitment of Th17 cells and the enhanced expression of IL-17 and recruitment of neutrophils [56]. Indeed, in the *Awat2* KO mouse there is a marked increase in the T-cell population that is marked by the expression of IL-17, suggesting the presence of Th17 cells involved in the recruitment of neutrophils to the meibomian gland. Studies of cultured skin keratinocytes have also shown that mechanical stretch can induce expression of IL-23 in keratinocytes, suggesting that in the *Awat2* KO mouse, dilation of the duct and mechanical stretching may lead to a similar increased expression of IL-23a, leading to recruitment of Th17 cells and acute inflammation [57]. Mechanical stretch also leads to increased keratinocyte proliferation, perhaps explaining the hyperplasia of the ductal epithelium in the Awat2 KO mouse. Besides the expression of Fabp5 and IL-23 in the ductal epithelial cells and presence of Th17 T-cells and expanded neutrophils, other psoriasis-like markers found in the *Awat2* KO mouse include S100a9 in the conjunctival and keratinocytes around the meibomian gland duct and a general increased expression of Lcn2.

Taken together, these findings support the novel hypothesis that obstruction of the meibomian gland that causes dilation of the duct induces a psoriasis-like syndrome, resulting in hyperplasia of the ductal epithelium combined with expression of IL-23a, which leads to Th17 T-cell activation, expression of IL-17, and recruitment of neutrophils. In support of this hypothesis, psoriasis is a known risk factor for the development of dry eye disease and MGD, with Psoriatic patients showing an increased incidence and severity of disease [58]. Given the observed severity of the inflammatory cell infiltration into the gland and conjunctiva by neutrophils and other CD45-positive cells it is likely that this inflammation may extend beyond the eyelid and affect the cornea and ocular surface. Although ocular surface changes have been noted previously in the *Awat2* KO mouse, including decreased tear breakup time, corneal surface damage, and inflammation, it has been assumed that these dry eye disease signs were the result of altered meibum affecting tear film function and causing ocular surface inflammation. In contrast, our findings suggest an alternative explanation that involves the meibomian gland in the initiation of an inflammatory response that has downstream effects on the ocular surface. Our finding that inflammatory infiltration of the meibomian gland is more severe in younger compared to older mice with decreased *IL-17a*- and *IL-23a*-expressing cells may be supportive of this alternative explanation, as mechanical stretching may plateau in adult mice along with *IL-23* signaling. Certainly, further study of the model is needed to understand the role of duct dilation and inflammation in causing dry eye disease.

5.   Summary

Overall, this is the first report that details the transcriptional dynamics of the meibomian gland of the eyelid under conditions of homeostasis and dysfunction associated with age and abnormal meibum quality. The findings support a model in which the meibomian gland under homeostatic conditions contain two distinct stem/progenitor cell populations (Meibocyte Stem and Ductal Stem) that give rise separately to the ductal epithelial and meibocyte populations (Fig. 9). While ductal cells differentiate to non-keratinized or keratinized epithelium, meibocyte stem cells give rise to basal acinar progenitor cells that are Krt5$^+$/Pparg$^-$ and then transitional meibocytes progenitor cells expressing Pparg prior to migrating into the acinar compartment similar to sebocytes [23]. Differentiating meibocytes within the acinar compartment appear to sequentially express lipogenic genes required for synthesis of meibum using a stratified differentiation program wherein cells first express Soat1 and Far2 and synthesize cholesterol esters and fatty alcohols (Meibocyte Diff 1 cells) and then express Awat2 (Meibocyte Diff 2 cells) and synthesize wax esters from fatty alcohols to produce mature meibum lipid.

Our studies also suggest that the responses of these two populations appear to be different under different dysfunctional states, leading either to decreased meibocyte growth with aging or increased ductal growth and hyperplasia with altered meibum quality. In the latter case, changes in meibum quality with loss of wax esters and increased cholesterol esters leading to increased meibum viscosity (inspissation) and duct obstruction causes dilation of the duct and mechanical stretching of the ductal epithelium that initiates a signaling cascade, similarly identified in psoriasis. This cascade may involve expression of Il-23a, S100a8/a9 and Lcn2by non-keratinized ductal epithelium and meibocytes and a downstream type 3 immune response involving Th-17 T-cells, Il-17 release and neutrophil infiltration (PMN).

Supplementary Material

Refer to Web version on PubMed Central for supplementary material.

Funding

References

[1]. Knop E, Knop N, Millar T, Obata H, Sullivan DA. The international workshop on meibomian gland dysfunction: report of the subcommittee on anatomy, physiology, and pathophysiology of the meibomian gland. Invest Ophthalmol Vis Sci 2011;52:1938–78. [PubMed: 21450915]

[2]. Linton RG, Curnow DH, Riley WJ. The meibomian glands: an investigation into the secretion and some aspects of the physiology. Br J Ophthalmol 1961;45:718–23. [PubMed: 18170726]

[3]. Mishima S, Maurice DM. The oily layer of the tear film and evaporation from the corneal surface. Exp Eye Res 1961;1:39–45. [PubMed: 14474548]

[4]. Hom MM, Martinson JR, Knapp LL, Paugh JR. Prevalence of Meibomian gland dysfunction. Optom Vis Sci 1990;67:710–2. [PubMed: 2234831]

[5]. Lemp MA, Nichols KK. Blepharitis in the United States 2009: a survey-based perspective on prevalence and treatment. Ocul Surf 2009;7:S1–14. [PubMed: 19383269]

[6]. Ong BL. Relation between contact lens wear and Meibomian gland dysfunction. Optom Vis Sci 1996;73:208–10. [PubMed: 8725025]

[7]. Ong BL, Larke JR. Meibomian gland dysfunction: some clinical, biochemical and physical observations. Ophthalmic Physiol Opt 1990;10:144–8. [PubMed: 2371060]

[8]. Foulks GN, Bron AJ. Meibomian gland dysfunction: a clinical scheme for description, diagnosis, classification, and grading. Ocul Surf 2003;1:107–26. [PubMed: 17075643]

[9]. Kitazawa K, et al. Impact of aging on the pathophysiology of dry eye disease: a systematic review and meta-analysis. Ocul Surf 2022;25:108–18. [PubMed: 35753664]

[10]. Nien CJ, et al. Effects of age and dysfunction on human meibomian glands. Arch Ophthalmol 2011;129:462–9. [PubMed: 21482872]

[11]. Nien CJ, et al. Age-related changes in the meibomian gland. Exp Eye Res 2009;89:1021–7. [PubMed: 19733559]

[12]. Widjaja-Adhi MAK, et al. Deficiency in Acyl-CoA:Wax Alcohol Acyltransferase 2 causes evaporative dry eye disease by abolishing biosynthesis of wax esters. FASEB J 2020;34:13792–808. [PubMed: 32851726]

[13]. Butovich IA, Wilkerson A. Dynamic changes in the gene expression patterns and lipid profiles in the developing and maturing meibomian glands. Int J Mol Sci 2022;23:7884. [PubMed: 35887230]

[14]. Stuart T, et al. Comprehensive integration of single-cell data. Cell 2019;177:1888–1902.e1821. [PubMed: 31178118]

[15]. Xie Z, et al. Gene set knowledge discovery with enrichr. Current Protocols 2021;1:e90. [PubMed: 33780170]

[16]. Qiu X, et al. Single-cell mRNA quantification and differential analysis with Census. Nat Methods 2017;14:309–15. [PubMed: 28114287]

[17]. Crow M, Paul A, Ballouz S, Huang ZJ, Gillis J. Characterizing the replicability of cell types defined by single cell RNA-sequencing data using MetaNeighbor. Nat Commun 2018;9:884. [PubMed: 29491377]

[18]. Aibar S, et al. SCENIC: single-cell regulatory network inference and clustering. Nat Methods 2017;14:1083–6. [PubMed: 28991892]

[19]. Stringer C, Wang T, Michaelos M, Pachitariu M. Cellpose: a generalist algorithm for cellular segmentation. Nat Methods 2021;18:100–6. [PubMed: 33318659]

[20]. Petukhov V, et al. Cell segmentation in imaging-based spatial transcriptomics. Nat Biotechnol 2022;40:345–54. [PubMed: 34650268]

[21]. Dries R, et al. Giotto: a toolbox for integrative analysis and visualization of spatial expression data. Genome Biol 2021;22:78. [PubMed: 33685491]

[22]. Satija R, Farrell JA, Gennert D, Schier AF, Regev A. Spatial reconstruction of single-cell gene expression data. Nat Biotechnol 2015;33:495–502. [PubMed: 25867923]

[23]. Veniaminova NA, et al. Distinct mechanisms for sebaceous gland self-renewal and regeneration provide durability in response to injury. 2023.

[24]. McMahon A, Lu H, Butovich IA. A role for ELOVL4 in the mouse meibomian gland and sebocyte cell biology. Invest Ophthalmol Vis Sci 2014;55:2832–40. [PubMed: 24677106]

[25]. Trapnell C, et al. The dynamics and regulators of cell fate decisions are revealed by pseudotemporal ordering of single cells. Nat Biotechnol 2014;32:381–6. [PubMed: 24658644]

[26]. Jin S, et al. Inference and analysis of cell-cell communication using CellChat. Nat Commun 2021;12:1088. [PubMed: 33597522]

[27]. Shao S, et al. Increased lipocalin-2 contributes to the pathogenesis of psoriasis by modulating neutrophil chemotaxis and cytokine secretion. J Invest Dermatol 2016;136:1418–28. [PubMed: 26979478]

[28]. Silva de Melo BM, et al. S100A9 drives the chronification of psoriasiform inflammation by inducing IL-23/type 3 immunity. J Invest Dermatol 2023;143:1678–1688.e1678. [PubMed: 36921684]

[29]. Gudjonsson JE, et al. Assessment of the psoriatic transcriptome in a large sample: additional regulated genes and comparisons with in vitro models. J Invest Dermatol 2010;130:1829–40. [PubMed: 20220767]

[30]. Li C, et al. Psoriasis-associated impairment of CCL27/CCR10-derived regulation leads to IL-17A/IL-22-producing skin T cell over-activation. The Journal of allergy and clinical immunology 2021;147:759–763.e759. [PubMed: 32533971]

[31]. Hotz C, et al. Intrinsic defect in keratinocyte function leads to inflammation in hidradenitis suppurativa. J Invest Dermatol 2016;136:1768–80. [PubMed: 27206704]

[32]. Butovich IA. Meibomian glands, meibum, and meibogenesis. Exp Eye Res 2017;163:2–16. [PubMed: 28669846]

[33]. Butovich IA, Lu H, McMahon A, Eule JC. Toward an animal model of the human tear film: biochemical comparison of the mouse, canine, rabbit, and human meibomian lipidomes. Invest Ophthalmol Vis Sci 2012;53:6881–96. [PubMed: 22918629]

[34]. Butovich IA, McMahon A, Wojtowicz JC, Bhat N, Wilkerson A. Effects of sex (or lack thereof) on meibogenesis in mice (Mus musculus): comparative evaluation of lipidomes and transcriptomes of male and female tarsal plates. Ocul Surf 2019;17:793–808. [PubMed: 30890458]

[35]. Borchman D, et al. Human meibum lipid conformation and thermodynamic changes with meibomian-gland dysfunction. Invest Ophthalmol Vis Sci 2011;52:3805–17. [PubMed: 21398284]

[36]. Borchman D, Yappert MC, Foulks GN. Changes in human meibum lipid with meibomian gland dysfunction using principal component analysis. Exp Eye Res 2010;91:246–56. [PubMed: 20546726]

[37]. Gutgesell VJ, Stern GA, Hood CI. Histopathology of meibomian gland dysfunction. Am J Ophthalmol 1982;94:383–7. [PubMed: 7124880]

[38]. Obata H. Anatomy and histopathology of human meibomian gland. Cornea 2002;21:S70–4. [PubMed: 12484702]

[39]. Reneker LW, Irlmeier RT, Shui YB, Liu Y, Huang AJW. Histopathology and selective biomarker expression in human meibomian glands. Br J Ophthalmol 2020;104:999–1004. [PubMed: 31585964]

[40]. Hampel U, et al. Serum-induced keratinization processes in an immortalized human meibomian gland epithelial cell line. PLoS One 2015;10:e0128096. [PubMed: 26042605]

[41]. Rho CR, et al. Expression of Acyl-CoA wax-alcohol acyltransferase 2 (AWAT2) by human and rabbit meibomian glands and meibocytes. Ocul Surf 2022;23:60–70. [PubMed: 34838721]

[42]. Ziemanski JF, Chen J, Nichols KK. Evaluation of cell harvesting techniques to optimize lipidomic analysis from human meibomian gland epithelial cells in culture. Int J Mol Sci 2020;21. [PubMed: 33375030]

[43]. Parfitt GJ, et al. Renewal of the holocrine meibomian glands by label-retaining, unipotent epithelial progenitors. Stem Cell Rep 2016;7:399–410.

[44]. Jester JV, Nicolaides N, Kiss-Palvolgyi I, Smith RE. Meibomian gland dysfunction. II. The role of keratinization in a rabbit model of MGD. Invest Ophthalmol Vis Sci 1989;30:936–45. [PubMed: 2470694]

[45]. Jester JV, Nicolaides N, Smith RE. Meibomian gland studies: histologic and ultrastructural investigations. Invest Ophthalmol Vis Sci 1981;20:537–47. [PubMed: 7194327]

[46]. Jester JV, Rajagopalan S, Rodrigues M. Meibomian gland changes in the rhino (hrrhhrrh) mouse. Invest Ophthalmol Vis Sci 1988;29:1190–4. [PubMed: 2458328]

[47]. Ohnishi Y, Kohno T. Polychlorinated biphenyls poisoning in monkey eye. Invest Ophthalmol Vis Sci 1979;18:981–4. [PubMed: 113362]

[48]. Parfitt GJ, Xie Y, Geyfman M, Brown DJ, Jester JV. Absence of ductal hyperkeratinization in mouse age-related meibomian gland dysfunction (ARMGD). Aging (Albany NY) 2013;5:825–34. [PubMed: 24259272]

[49]. Gupta PK, et al. Meibomian gland dysfunction: a dermatological perspective on pathogenesis and treatment outlook. Clin Ophthalmol 2021;15:4399–404. [PubMed: 34785886]

[50]. Nuwormegbe S, et al. Induction of meibocyte differentiation by three-dimensional, matrigel culture of immortalized human meibomian gland epithelial cells to form acinar organoids. Ocul Surf 2022;26:271–82. [PubMed: 36341959]

[51]. Butovich IA, Wilkerson A. Dynamic changes in the gene expression patterns and lipid profiles in the developing and maturing meibomian glands. Int J Mol Sci 2022;23. [PubMed: 36613467]

[52]. Suhalim JL, et al. Effect of desiccating stress on mouse meibomian gland function. Ocul Surf 2014;12:59–68. [PubMed: 24439047]

[53]. Jester BE, Nien CJ, Winkler M, Brown DJ, Jester JV. Volumetric reconstruction of the mouse meibomian gland using high-resolution nonlinear optical imaging. Anat Rec 2011;294:185–92.

[54]. Sawai M, et al. Erratum: diverse meibum lipids produced by Awat1 and Awat2 are important for stabilizing tear film and protecting the ocular surface. iScience 2021;24:103160. [PubMed: 34622178]

[55]. Nowowiejska J, Baran A, Flisiak I. Fatty acid-binding proteins in psoriasis-A review. Metabolites 2022;12. [PubMed: 36676936]

[56]. Hawkes JE, Yan BY, Chan TC, Krueger JG. Discovery of the IL-23/IL-17 signaling pathway and the treatment of psoriasis. J Immunol 2018;201:1605–13. [PubMed: 30181299]

[57]. Qiao P, et al. Mechanical stretch exacerbates psoriasis by stimulating keratinocyte proliferation and cytokine production. J Invest Dermatol 2019;139:1470–9. [PubMed: 30641039]

[58]. Wu PC, et al. Psoriasis and dry eye disease: a systematic review and meta-analysis. Dermatology 2022;238:876–85. [PubMed: 35299172]
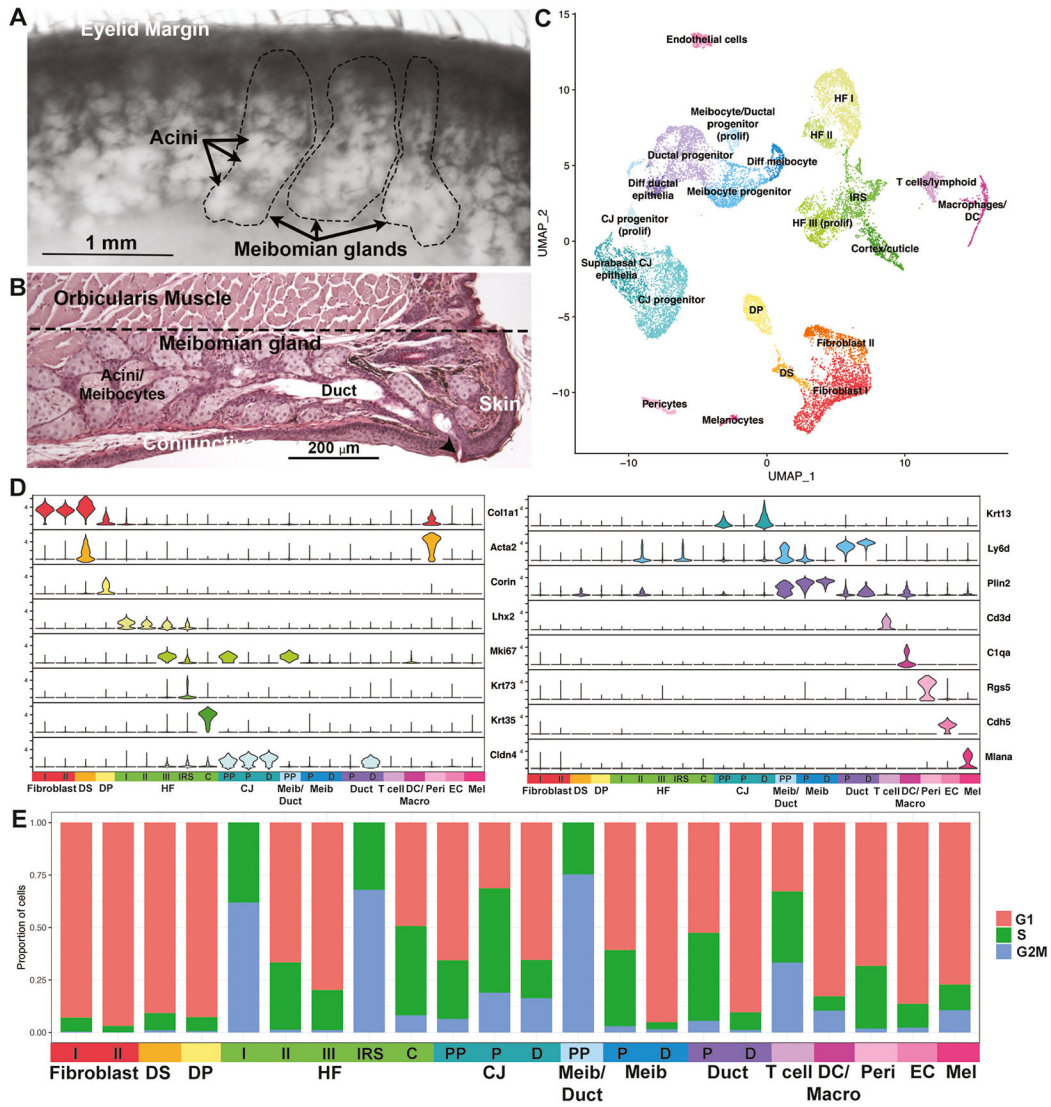
Fig. 1.
Identifying cell type composition in the murine eyelid. A) The meibomian glands (Dash Lines) can be seen as a row of white structures embedded in the distal eyelid that extend from the Eyelid Margin and are comprised of clusters of small round acini. B) H&E-stained tissue section of eyelid from a normal wild type mouse showing the meibomian gland underlying the Orbicularis Muscle. The gland has a blind ended central duct (Duct) connecting acini to the gland orifice (Arrowhead) at the junction between the skin and conjunctiva. C) Uniform manifold approximation and projection (UMAP) visualization of 3 datasets integrated. Each dot represents a single cell (n = 16,922). D) Violin plot showing marker gene expression for identified cell types. E) Proportion of cells in each cell cycle phase (as assigned by the CellCycleScoring function in Seurat) split by cell type clusters.
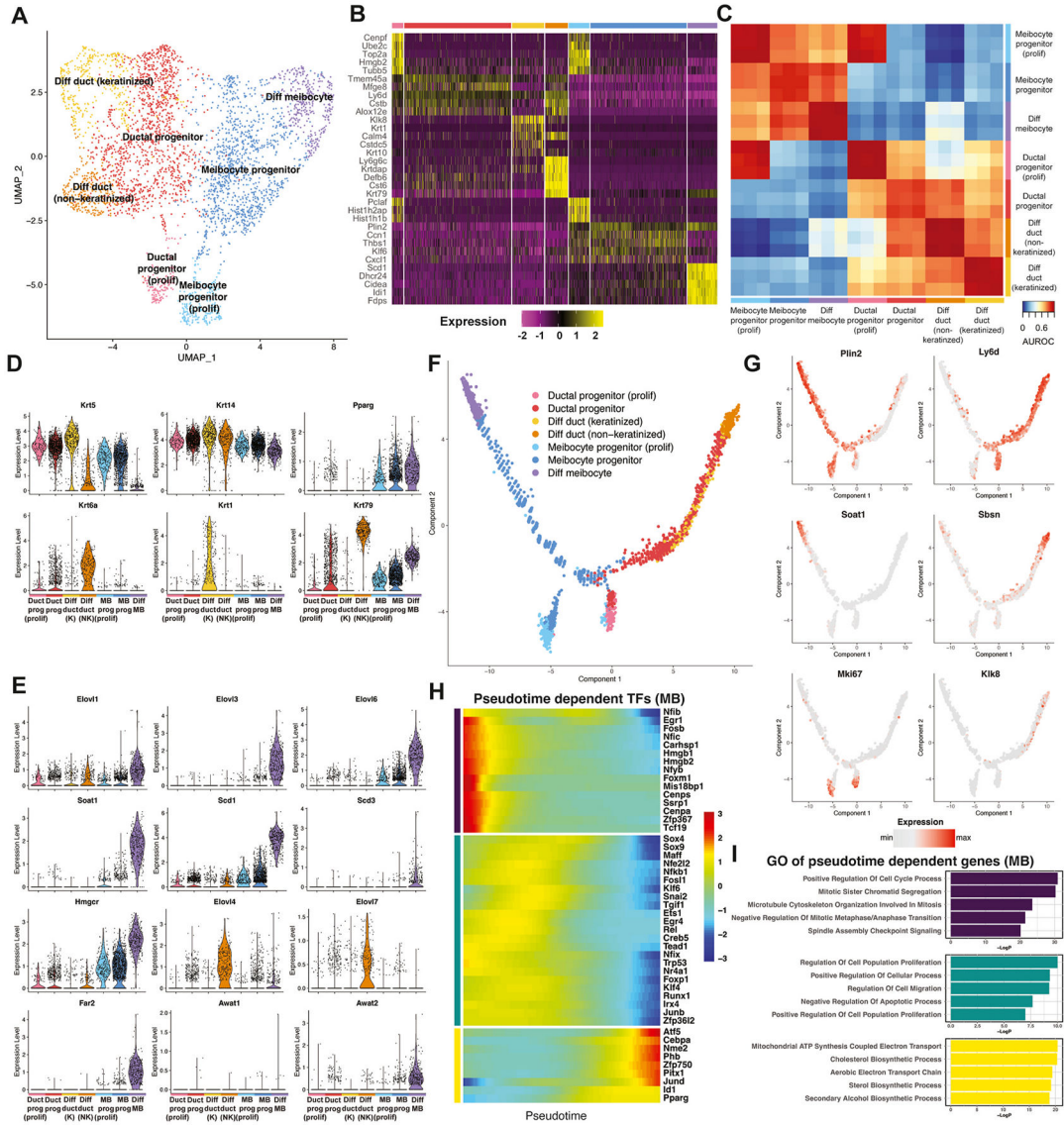
Fig. 2.

Identifying the cell type composition and differentiation programs in the healthy meibomian gland. A) UMAP visualization of meibomian gland epithelial clusters. Each dot represents a single cell (n = 3741). B) Heatmap of top differentially expressed genes for each cluster. C) Heatmap of AUROC scores between meibomian gland clusters based on the highly variable gene set using MetaNeighbor. D) Violin plots showing expression of keratins and Pparg in the meibomian gland. E) Violin plots showing expression of lipid associated genes in the meibomian gland. F) Monocle trajectory for meibomian gland epithelial clusters. G) Pseudotime trajectory with cells colored by marker gene expression. H) Heatmap dividing the expression of top meibocyte pseudotime dependent transcription factors into three groups. I) Gene ontology results for three groups of meibocyte pseudotime dependent genes.
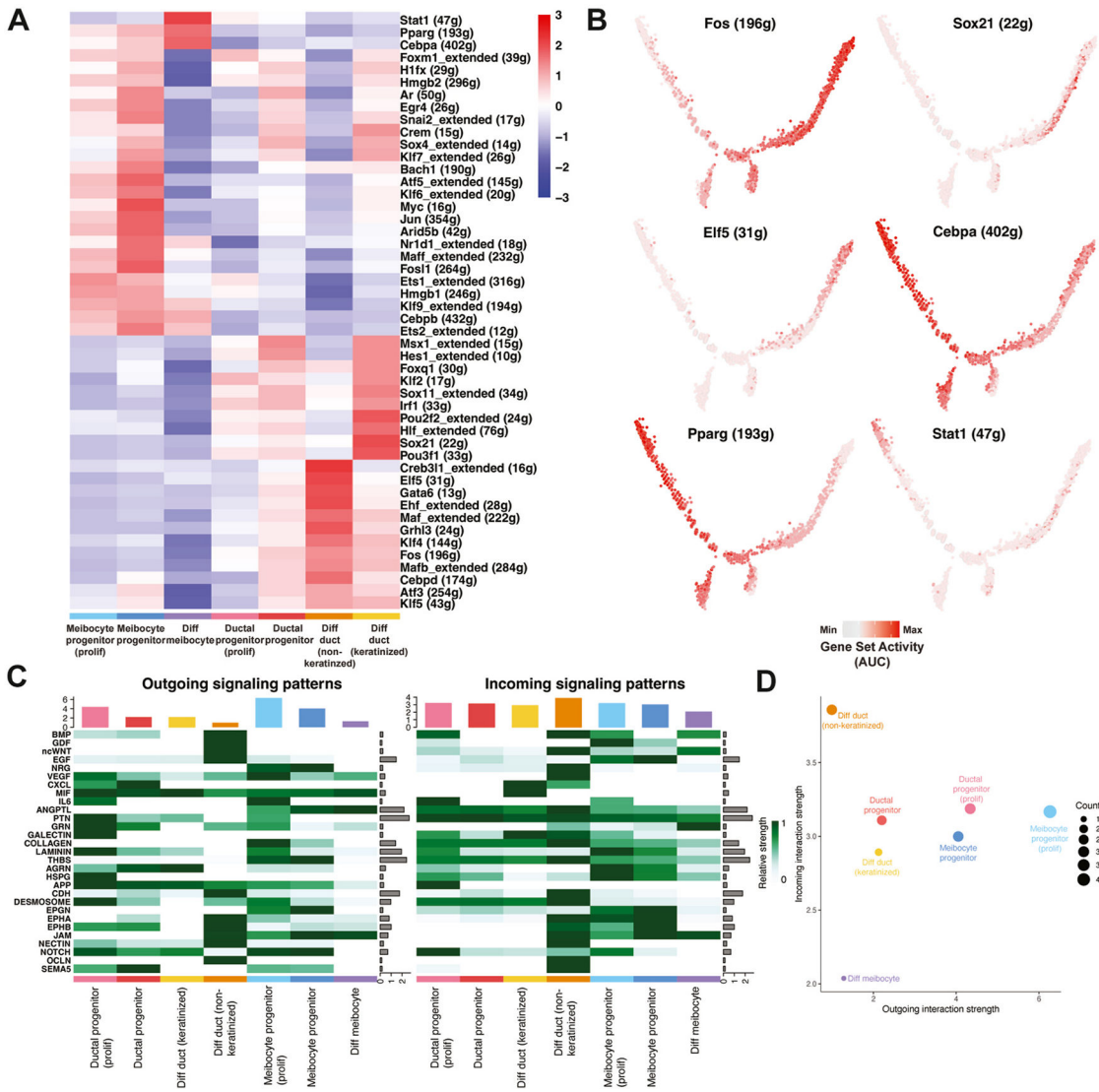
Fig. 3.
Meibomian gland differentiation is marked by distinct transcription factor and signaling networks. A) Heatmap showing SCENIC results for the meibomian gland clusters. B) Pseudotime trajectory with cells colored by SCENIC gene set activity. C) Heatmaps showing incoming and outgoing patterns of top signaling pathways in the meibomian gland populations using CellChat. D) Scatterplot showing separation of meibomian gland populations into general senders or receivers of signals.
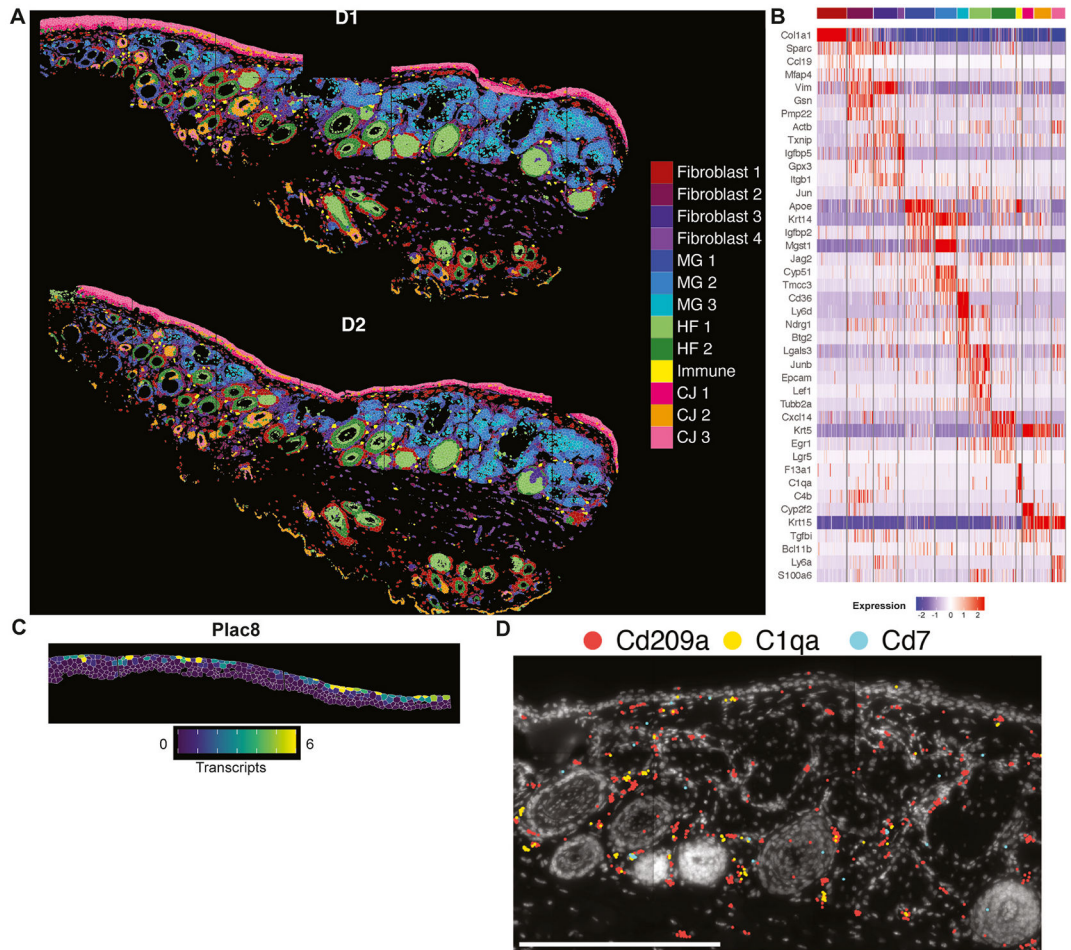
Fig. 4.
Spatial transcriptomics maps the healthy murine eyelid and localizes novel spatial populations. A) Results of joint clustering of the two replicates displayed on cell segmentation (n = 14,576). B) Heatmap showing the top marker genes for each identified cluster. C) Expression of Plac8 shown on cell segmentation of the conjunctiva colored by number of transcripts per cell. D) Transcripts of immune population markers displayed on the DAPI image of the eyelid. Scale bar indicates 300um.
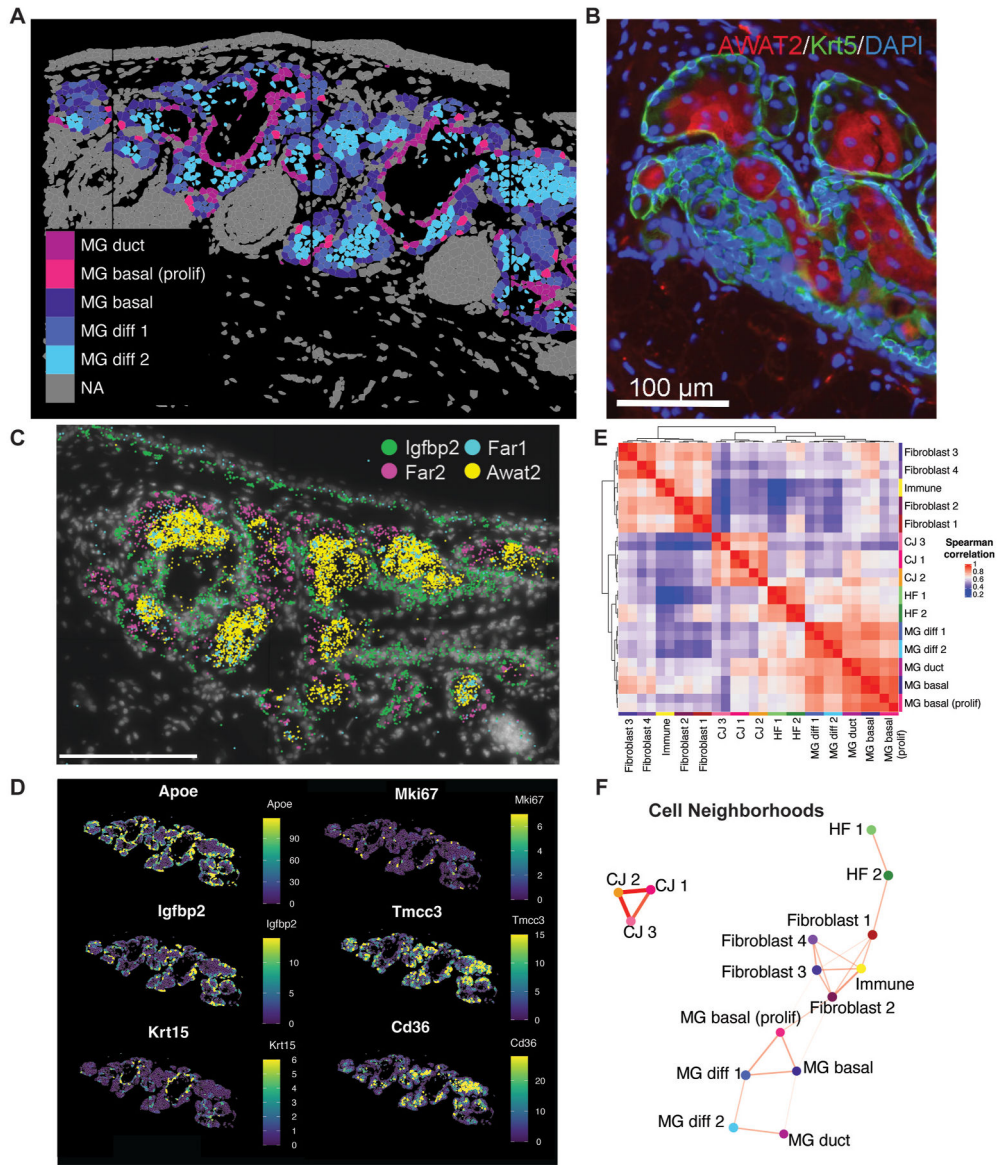
Fig. 5.
Gradual meibocyte differentiation in the murine eyelid. A) Cell segmentation of meibomian gland (n = 2513) colored by the results of subclustering. Surrounding cell types shown in grey. B) Immunohistochemical staining for Awat2 (red) in the mouse meibomian gland shows segmental staining for expression of Awat2 primarily in the central region of the acini. Basal meibocytes are identified by positive Krt5 expression (green), cell nuclei are labeled with DAPI (blue). C) Transcripts of four meibocyte differentiation markers displayed on the DAPI image of themeibomian gland. Scale bar indicates 150um. D) Marker genes for each of the five identified meibomian gland projected on the cell segmentation colored by number of transcripts per cell. E) Heatmap showing Spearman correlation of gene expression of the spatial clusters. F) Cell neighborhoods determined by spatial proximity of cell types.
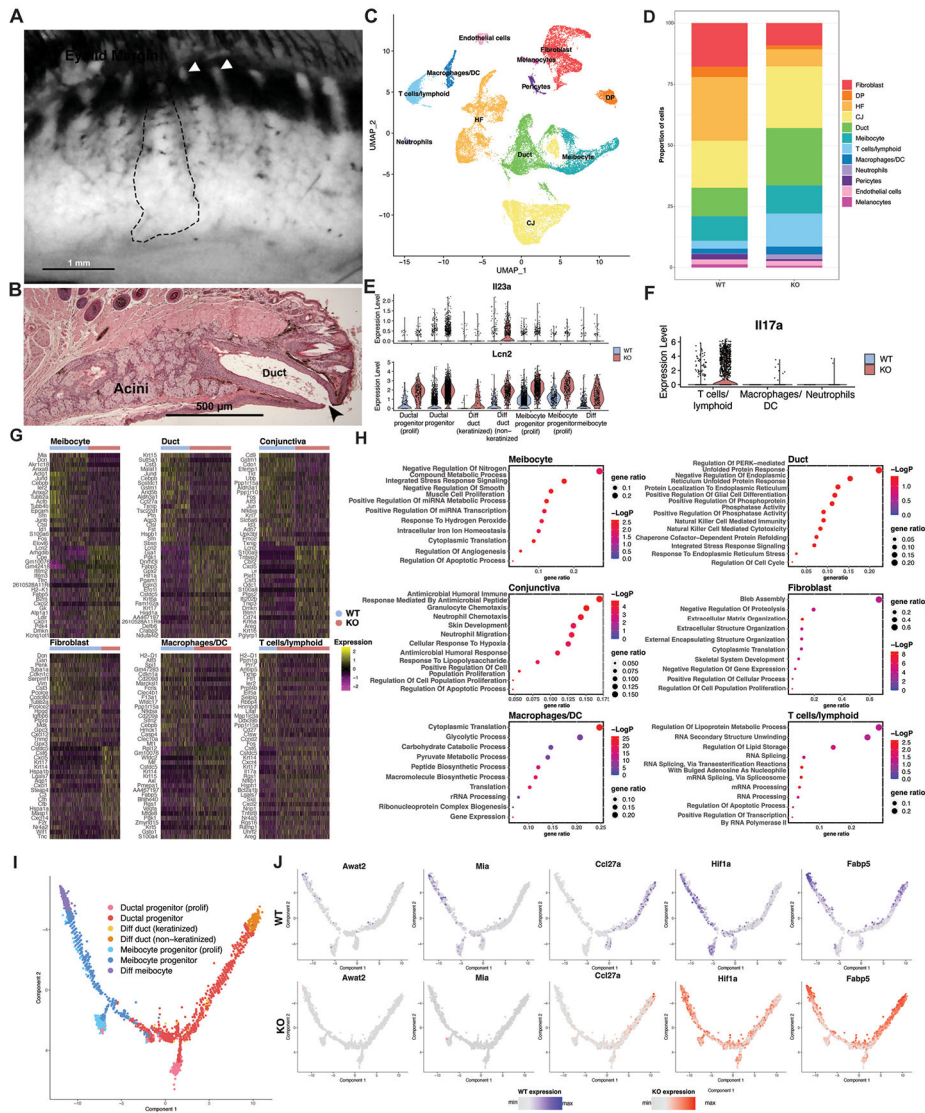
Fig. 6.
Dysregulation of meibomian gland differentiation and immunological processes in the *Awat2* KO. A) Eyelid of the *Awat2* KO contains enlarged meibomian glands (Dash line) with plug meibomian gland orfices (Arrowhead). B) H&E stained eyelid section (a) showing extreme dilation of the meibomian gland duct with ductal epithelial hyperplasia (Duct) and enlarged orifice (Arrowhead). C) UMAP visualization showing the integration of the *Awat2* WT and KO datasets. Each dot represents a single cell (n = 29,277). D) Bar plot showing proportion of each cell type by status. E) Violin plots of Il23a and Lcn2 in the meibomian gland populations split by status. F) Violin plots of Il17a in the immune populations split by status. G) Heatmaps displaying cell type specific top differentially expressed genes for meibocytes, ductal epithelia, conjunctiva, fibroblasts, macrophages/DC, and T cell/lymphoid. H) Dot plot displaying top cell type specific gene ontology terms based on the differentially expressed genes shown in G. I) Monocle trajectory for meibomian
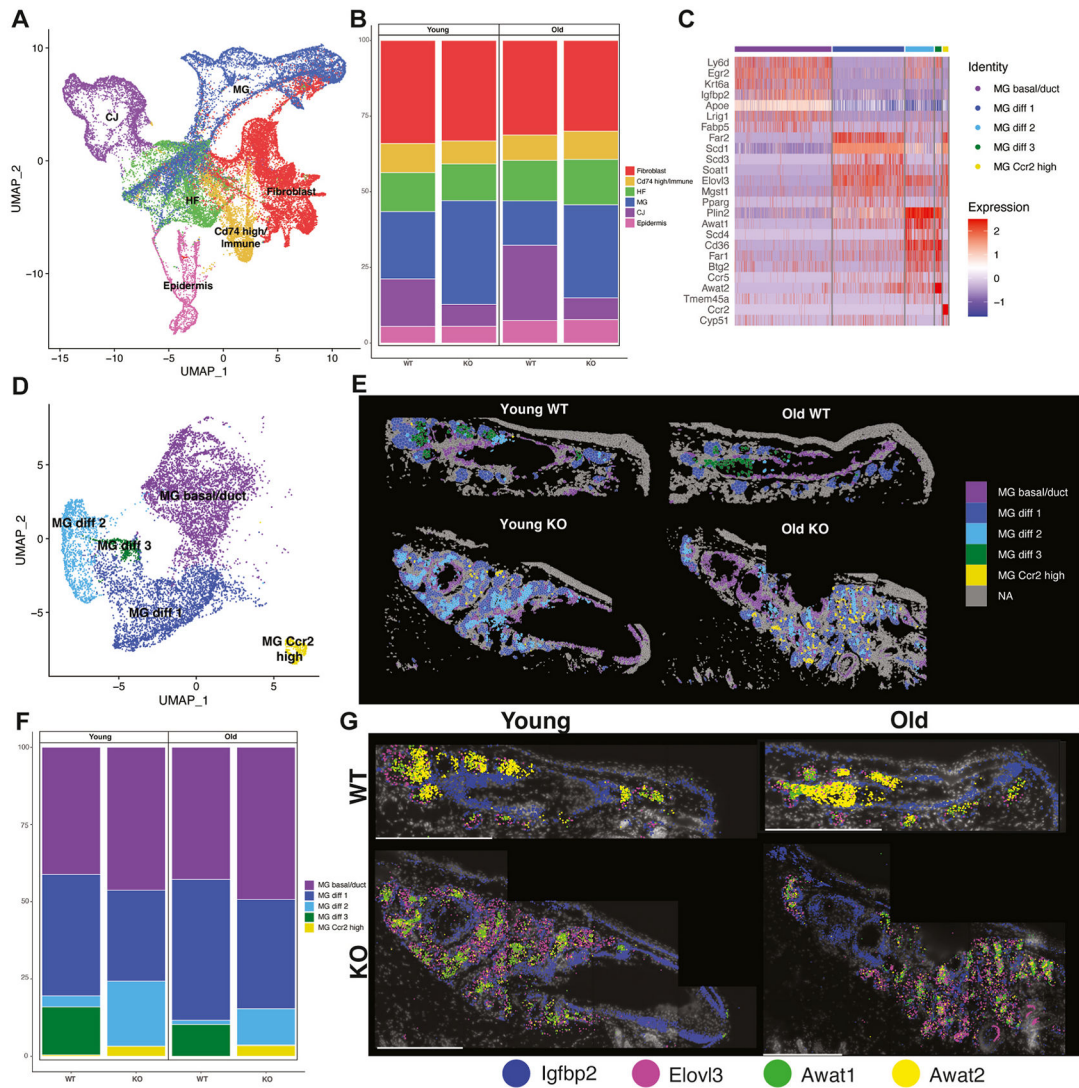
gland epithelial clusters. J) Differential genes projected onto the meibomian gland Monocle trajectories for the WT (top) and KO (bottom).

Fig. 7.
Spatial transcriptomic profiling of the eyelid during meibomian gland dysfunction in young and aged mice reveals alterations in meibocyte differentiation. A) UMAP of the integrated spatial transcriptomic dataset colored by general cell types ($n = 36,668$ cells). B) Proportions of cell types in the spatial dataset split both by young and old and *Awat2* KO and wildtype status. C) Heatmap showing top markers of 5 meibomian gland specific clusters. D) UMAP showing results of meibomian gland sub-clustering ($n = 9592$). E) Results of clustering displayed on cell segmentation. Cells colored by the 5 identified meibomian gland cell types, with other cell types in grey. F) Proportions of the meibomian cell types in the spatial dataset split both by young and old and *Awat2* KO and wildtype status. G) Individual transcripts for *Igfbp2*, *Elovl3*, *Awat1*, and *Awat2* shown on DAPI staining for each condition.
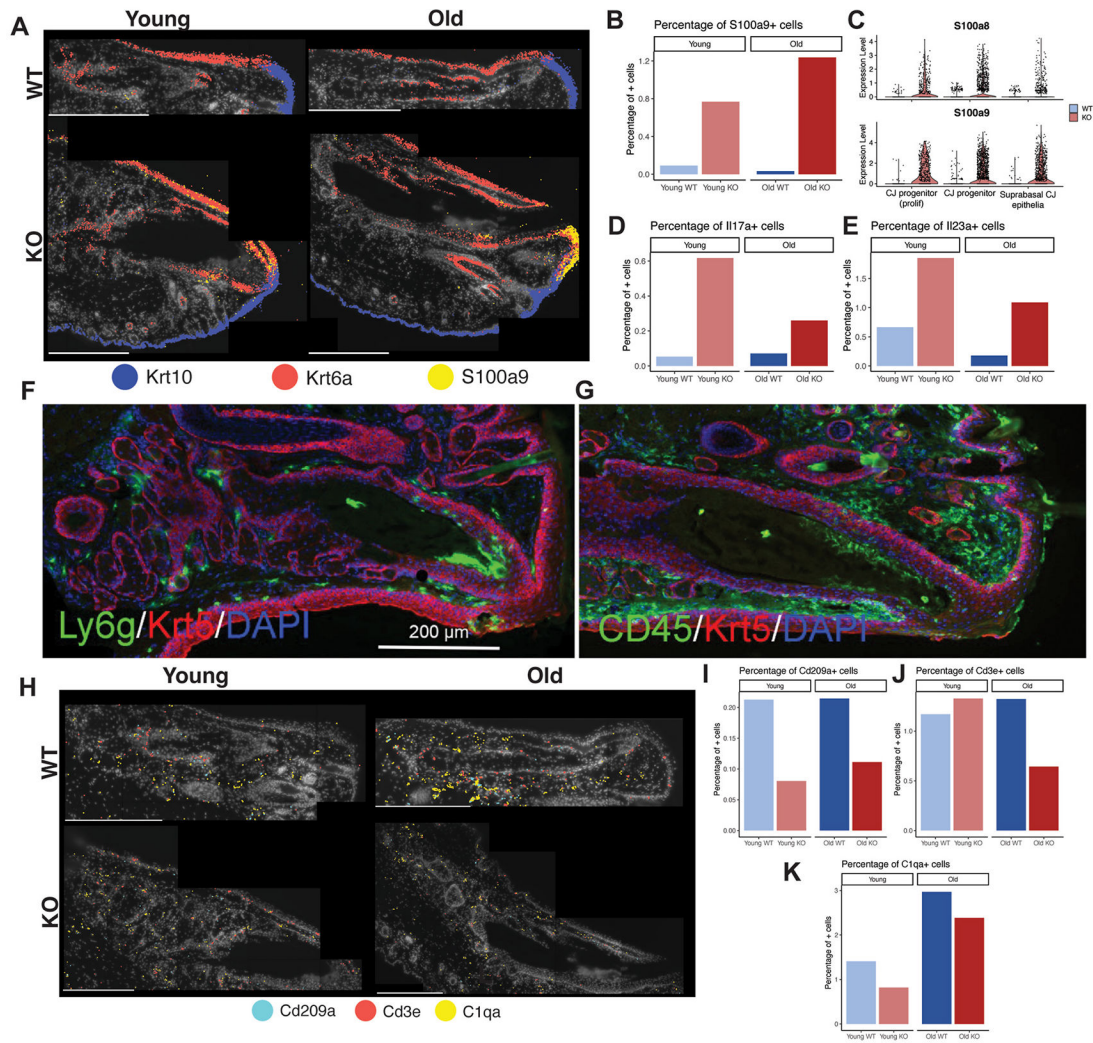
Fig. 8.

Localizing a spatially distinct inflammatory environment in the murine eyelid during meibomian gland dysfunction. A) Individual transcripts for *Krt10* (epidermis), *Krt6a* (conjunctiva), and *S100a9* shown on DAPI staining for each condition Scale bars indicate 300um. B) Bar plot showing proportion of cells expressing >1 transcript of *S100a9* in each condition. C) Violin plots of the single cell data showing expression of *S100a8* and *S100a8* in the conjunctiva populations split by condition. D) Bar plot showing proportion of cells near the meibomian gland expressing 1 transcript of *Il17a* each condition. E) Bar plot showing proportion of cells near the meibomian gland expressing 1 transcript of *Il23a* in each condition. F) Immunohistochemical staining of Awat2 knockout mouse eyelid stained for antibodies against neutrophils (Ly6g-Green) and G) bone marrow derived cells (CD45-Green), counter stained for basal cell (Krt5, red) and nuclei marker (DAPI, blue). H) Individual transcripts for immune cell markers *Cd209a*, for dendritic cells, *Cd3e*, for T cells, and *C1qa*, for macrophages shown on DAPI staining for young and old WT. Scale bars indicate 300um. I-K) Bar plots showing proportion of cells near the meibomian gland expressing >1 transcript of immune cell markers.
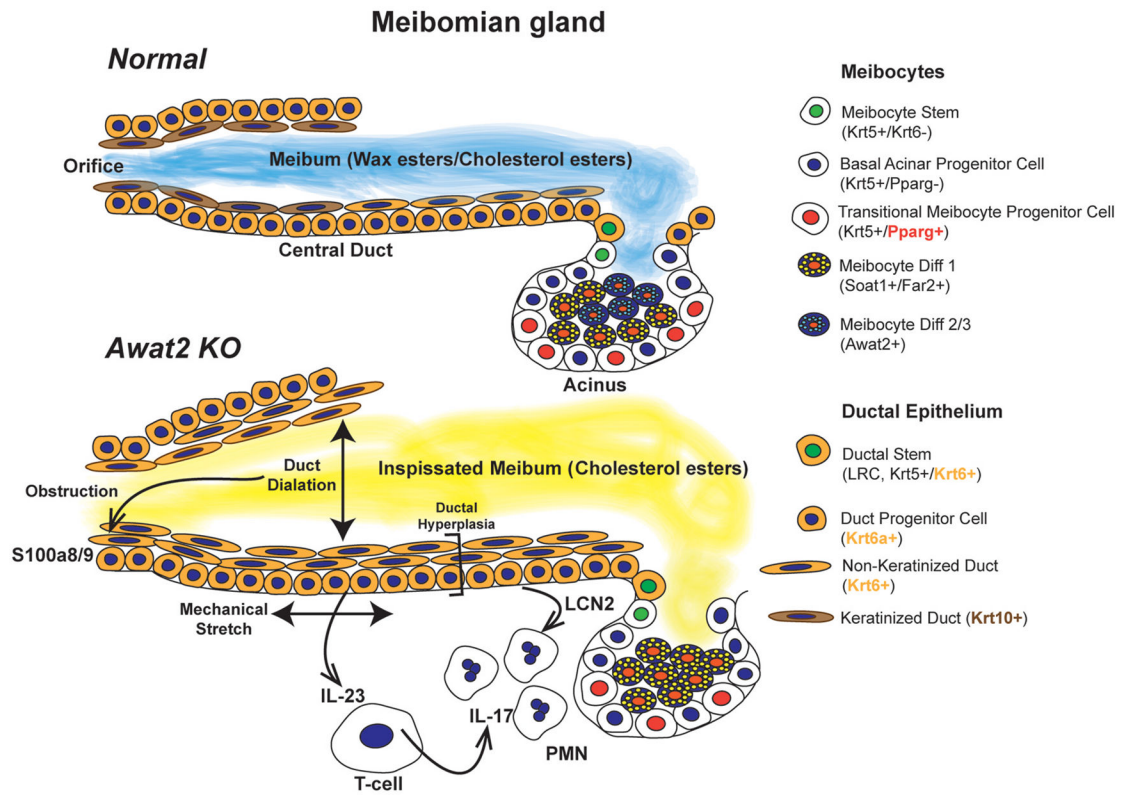
Fig. 9.
Graphical Diagram of the signal cell and spatial transcriptomic findings during normal meibomian gland homeostasis and dysfunction in normal and the Awat2 KO mouse.